



Article

Research on Fano Resonance Sensing Characteristics Based on Racetrack Resonant Cavity

Yaxin Yu, Jiangong Cui , Guochang Liu , Rongyu Zhao, Min Zhu, Guojun Zhang * and Wendong Zhang

State Key Laboratory of Dynamic Testing Technology, North University of China, Taiyuan 030051, China; s1906103@st.nuc.edu.cn (Y.Y.); jgcui@nuc.edu.cn (J.C.); b200611@st.nuc.edu.cn (G.L.); s2006241@st.nuc.edu.cn (R.Z.); s2006170@st.nuc.edu.cn (M.Z.); wdzhang@nuc.edu.cn (W.Z.)

* Correspondence: zhangguojun1977@nuc.edu.cn; Tel.: +86-13834680208

Abstract: To reduce the loss of the metal–insulator–metal waveguide structure in the near-infrared region, a plasmonic nanosensor structure based on a racetrack resonant cavity is proposed herein. Through finite element simulation, the transmission spectra of the sensor under different size parameters were analyzed, and its influence on the sensing characteristics of the system was examined. The analysis results show that the structure can excite the double Fano resonance, which has a distinctive dependence on the size parameters of the sensor. The position and line shape of the resonance peak can be adjusted by changing the key parameters. In addition, the sensor has a higher sensitivity, which can reach 1503.7 nm/RIU when being used in refractive index sensing; the figure of merit is 26.8, and it can reach 0.75 nm/°C when it is used in temperature sensing. This structure can be used in optical integrated circuits, especially high-sensitivity nanosensors.

Keywords: metal-insulator-metal; racetrack resonant cavity; Fano resonance; refractive index sensing; temperature sensing



Citation: Yu, Y.; Cui, J.; Liu, G.; Zhao, R.; Zhu, M.; Zhang, G.; Zhang, W. Research on Fano Resonance Sensing Characteristics Based on Racetrack Resonant Cavity. *Micromachines* **2021**, *12*, 1359. <https://doi.org/10.3390/mi12111359>

Academic Editor: Aiqun Liu

Received: 10 October 2021
Accepted: 27 October 2021
Published: 3 November 2021

Publisher's Note: MDPI stays neutral with regard to jurisdictional claims in published maps and institutional affiliations.



Copyright: © 2021 by the authors. Licensee MDPI, Basel, Switzerland. This article is an open access article distributed under the terms and conditions of the Creative Commons Attribution (CC BY) license (<https://creativecommons.org/licenses/by/4.0/>).

1. Introduction

Surface plasmon polaritons (SPPs) are evanescent waves propagating along the surface of a metal, formed by the coupling of free electrons and photons on the metal's surface [1–5]. They propagate along the metal–medium surface and decay exponentially on both sides vertical to the interface. SPPs can overcome the limitations of the traditional optical diffraction limit and manipulate light waves in the sub-wavelength range; thus, they are widely applied in highly integrated nano-optoelectronic devices, such as nanosensors [6,7], filters [8–10], and waveguide modulators [11].

In recent years, the plasmon-induced transparency (PIT) [12], plasmon-induced absorption (PIA) [13], and Fano resonance [14] in surface plasmon nano-integrated sensor devices have attracted considerable research attention in the field of nano-integration. Among them, Fano resonance [15] is a phenomenon in which zero absorption occurs in the absorption spectrum, owing to the coupling interference effect between the continuous and discrete state energy levels. This interference effect exhibits asymmetric resonance that is different from the traditional Lorentz line spectrum. Because this asymmetrical Fano resonance spectrum has sharp lines, low radiation loss, and the resonance frequency is highly correlated with the refractive index and structural parameters of the filling material, it can be applied to the field of nanosensing with a higher figure of merit (FOM) and sensitivity (S) [16,17]. Therefore, Fano resonance is widely used in sensors [18], optical switches [19], slow light devices [20], and other fields.

In recent years, nanosensor structures of different shapes based on Fano resonance have been proposed by researchers, such as cup cavity [21], splitting ring cavity [22], notched cavity [23], and multiple ring cavity [24]. These structures can easily integrate and contact the sensing medium. Improving these structures to enhance sensitivity has increasingly become a major focus for researchers. For example, Liu et al. designed a sensor

structure with a short rod and a cup-shaped resonant cavity coupling [21], which serves as a refractive index sensor with a sensitivity of 600 nm/RIU. Zhang et al. proposed a refractive index sensor structure coupled with a tooth-shaped cavity [22], whose sensitivity reached 1200 nm/RIU, whereas Liu et al. analyzed a sensor structure coupled with a hexagonal resonant cavity [25] as a refractive index sensor that achieved a sensitivity of 937 nm/RIU. Chen et al. proposed a sensing system coupled with a rectangular resonant cavity [26] with a temperature-sensing sensitivity of 0.225 nm/°C. Chen et al. discussed temperature-sensing characteristics based on the ring resonant cavity [27], the sensitivity of which reached 0.31 nm/°C.

A metal–insulator–metal (MIM) waveguide coupled racetrack resonant cavity (RTRC) nanosensor with a baffle is proposed to reduce the loss of the MIM waveguide structure in the near-infrared region. To enhance the sensitivity of the sensor, defects are introduced into the structure to destroy its symmetry. The structure proposed in this study is simple, sensitive, and easy to manufacture. It is not necessary to change both the horizontal and vertical sizes of the ring cavity in the racetrack resonant cavity. The size of the raceway can be adjusted to meet the requirements of some special-sized devices. The influence of the structural parameters and the refractive index of the surrounding medium on the transmission characteristics is studied using the finite element method. Finally, the structural parameters are optimized, and a high sensitivity and figure of merit (FOM) are obtained. The structure potentially has great applications in optical communications and high-density integrated optics, especially in nano-optical sensing.

2. Model Building and Theory

2.1. Model Building

The proposed RTRC structure and its geometric parameters are illustrated in Figure 1. The structure consists of a baffled MIM waveguide and a racetrack resonator. [28], It can be fabricated by electron beam lithography and a stripping process during the experimental preparation, which comprises the following steps: (1) a metal layer is plated on the substrate—non-absorbent materials such as silicon dioxide can be selected as the substrate; (2) the waveguide structure is etched onto the metal layer using electron beam lithography and a stripping process [29,30]. The blue part in Figure 1 represents metallic Ag, and the white part represents the air medium. The relative permittivity of air, $\epsilon_d = 1$, and the relative permittivity of Ag are related to the frequency of the incident light. The dielectric constants calculated by the Debye-Drude model are in good agreement with experimental data in the red and near-infrared portions of visible light (600 nm–2000 nm), According to the Debye-Drude dispersion model [31]:

$$\epsilon(\omega) = \epsilon_\infty + \frac{\epsilon_s - \epsilon_\infty}{1 + i\omega\tau} + \frac{\sigma}{i\omega\epsilon_0} \quad (1)$$

where ϵ_0 represents the dielectric constant in a vacuum; ω represents the angular frequency of the incident light waves in a vacuum; ϵ_∞ represents an infinite dielectric constant, where $\epsilon_\infty = 3.8344$; ϵ_s represents the static dielectric constant, where $\epsilon_s = -9530.5$; τ represents the damping coefficient, $\tau = 7.35 \times 10^{-15}$ s; σ represents Ag conductivity, $\sigma = 1.1486 \times 10^7$ S/m.

A two-dimensional geometric model was established using the finite element (FEM) software COMSOL Multiphysics 5.5, and the width of the MIM waveguide and racetrack resonant cavity was set to $w = 50$ nm to ensure that only the basic transverse magnetic mode (TM₀) was supported [32]. The length of the racetrack was set to $L = 120$ nm, and the outer diameter of the resonant cavity was $R = 140$ nm. The relationship between the outer diameter R and the inner diameter r was $R = r + 50$ nm, the baffle width was $d = 20$ nm, and the coupling distance was $g = 10$ nm. The boundary conditions around the structure are set as a perfect matching layer (PML) with a thickness of 100 nm. The incident light enters from the left port of the model and is output from the right port. The grid adopts ultra-fine grid, the parameterized scanning interval is 1 nm, and the electromagnetic wave frequency

domain analysis module is used to numerically analyze the transmission spectrum and mode field distribution of the sensor system.

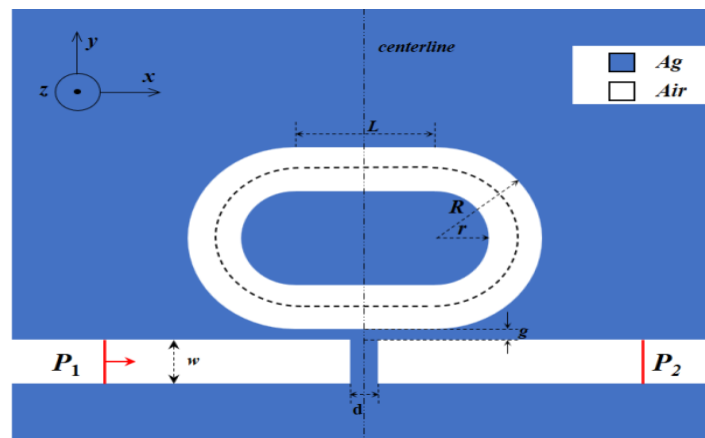


Figure 1. Schematic diagram of two-dimensional structure of plasmonic nanosensor.

2.2. Fano Resonance Principle Analysis

Firstly, the effect of the introduced racetrack structure is analyzed by simulation. The transmission spectrum of the coupling ring on the side of the MIM waveguide without the baffle, and that of the coupling ring and the coupled RTRC on the MIM waveguide side are shown in Figure 2a. The analyzed structure diagram is shown in Figure 2b,c. Compared with the circular ring, the RTRC transmission spectrum has more transmittance drop valleys, and new resonance modes appear at $\lambda = 700 \text{ nm}$ and $\lambda = 1365 \text{ nm}$, which are expressed as $m = 2$ and $m = 1$, respectively.

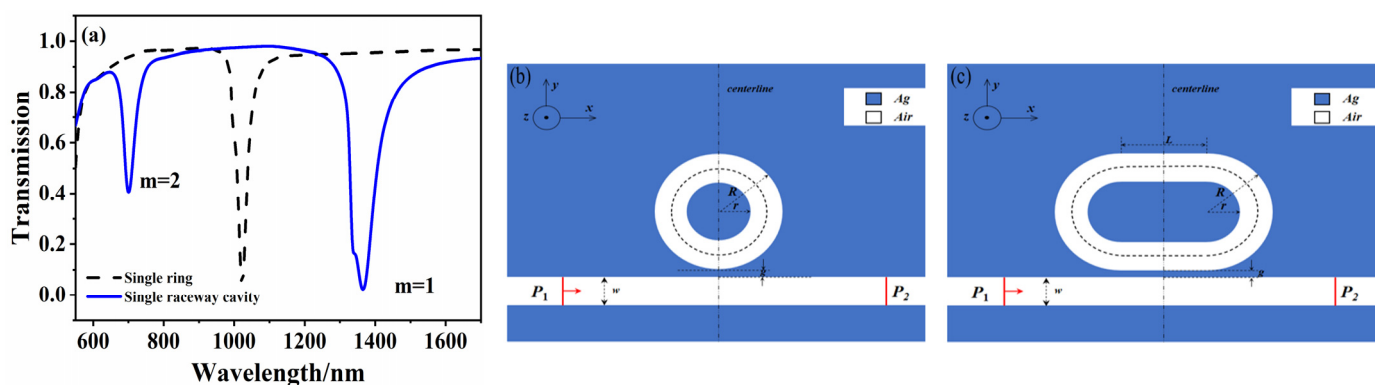


Figure 2. Comparison of transmittance spectrum between a circular ring and a RTRC side-coupled to a bus waveguide (a) Transmission pattern. (b) Schematic diagram of the structure of the ring. (c) schematic diagram of the structure of the raceway cavity.

Based on the coupled mode theory (CMT) [25], the mechanism of double Fano resonance is analyzed. The resonant amplitudes of the two resonant modes in the racetrack resonant cavity are represented by f_1 and f_2 , and normalized to the energy in the resonant cavity; S_{1+} and S_{2+} respectively represent the mode field amplitudes of the incident light at the incident port and the output port, S_{1-} and S_{2-} respectively represent the mode field amplitude of the light emitted from the incident port and the output port. With the change of time, the amplitude of the transmitted wave in the resonant cavity is [26]:

$$j\omega f_1 = \left(j\omega_1 - \frac{1}{\tau_{o1}} - \frac{1}{\tau_{e1}} \right) f_1 + k_1(S_{1+} + S_{2+}) \quad (2)$$

$$j\omega f_2 = \left(j\omega_2 - \frac{1}{\tau_{o2}} - \frac{1}{\tau_{e2}} \right) f_2 + k_2(S_{1+} + S_{2+}) \quad (3)$$

wherein, ω is the angular frequency of the incident light, $\omega_{1,2}$ corresponds to the resonant frequencies of the two resonant modes, $\frac{1}{\tau_{oi}}$ ($i = 1, 2$) represents the natural frequencies of the two modes of the resonant cavity, and $\frac{1}{\tau_{ei}}$ ($i = 1, 2$) corresponds to the amplitude attenuation of the two modes of the resonant cavity respectively coupled to the waveguide, and k_i ($i = 1, 2$) correspond to the input coupling coefficients of SPPs wave propagating forward and backward in the waveguide respectively. According to the law of conservation of energy [27], the output wave can be expressed as:

$$\begin{pmatrix} S_{1-} \\ S_{2-} \end{pmatrix} = C \begin{pmatrix} S_{1+} \\ S_{2+} \end{pmatrix} + k \begin{pmatrix} f_1 \\ f_2 \end{pmatrix} \quad (4)$$

wherein, C represents the scattering matrix directly coupled between the incident wave and the outgoing wave at the baffle in the waveguide structure. The expression is:

$$C = \begin{pmatrix} r & jt \\ jt & r \end{pmatrix} \quad (5)$$

wherein, t and r respectively correspond to the coefficients of the transmission amplitude and reflection amplitude, and $r + t = 1$; k is the coupling matrix between the output wave and the output port, and the specific expression is as follows:

$$k = \begin{pmatrix} -k_1^* & k_2^* \\ -k_1^* & -k_2^* \end{pmatrix} \quad (6)$$

From the time-reversal composability and the law of conservation of energy, we can get: $k_1 = \sqrt{1/\tau_{e1}}e^{j\theta_1}$, $k_2 = \sqrt{1/\tau_{e2}}e^{j\theta_2}$. Wherein, θ_1 and θ_2 respectively correspond to the phase coupling coefficients of the two coupling modes. The light transmission passes through the waveguide structure system, and the transmission spectrum amplitude is defined as $t(\omega) = S_{2-}/S_{1+}$. The calculation expression of the transmittance is:

$$T(\omega) = |t(\omega)|^2 = \left| jt - \frac{\frac{1}{\tau_{e1}}}{j(\omega - \omega_1) + \frac{1}{\tau_{o1}} + \frac{1}{\tau_{e1}}} - \frac{\frac{1}{\tau_{e2}}}{j(\omega - \omega_2) + \frac{1}{\tau_{o2}} + \frac{1}{\tau_{e2}}} \right|^2 \quad (7)$$

From Equation (6), it can be concluded that in the absence of a baffle $r = 0$, $t = 1$, and $\frac{1}{\tau_{o1}}, \frac{1}{\tau_{o2}}, \frac{1}{\tau_{e1}}$ and $\frac{1}{\tau_{e2}}$ are all constants, which are far less than $|j(\omega - \omega_{1,2})|$ ($\omega \neq \omega_{1,2}$). At this time, the transmittance is larger, and when the incident light frequency ω increases, its value is close to or equal to $\omega_{1,2}$, the transmittance suddenly drops sharply, forming two narrower discrete spectra. Therefore, compared with the regular ring structure, this study attributed the emergence of the new resonance mode to the introduced racetrack structure.

As shown in Figure 3, to verify the effect of the introduced baffle, a silver baffle was inserted into the MIM waveguide, where the width of the baffle was 20 nm and the other parameters were the same as those in Figure 2b. The entire sensor system was formed using the RTRC. The transmission spectra under different placement conditions are presented in Figure 3.

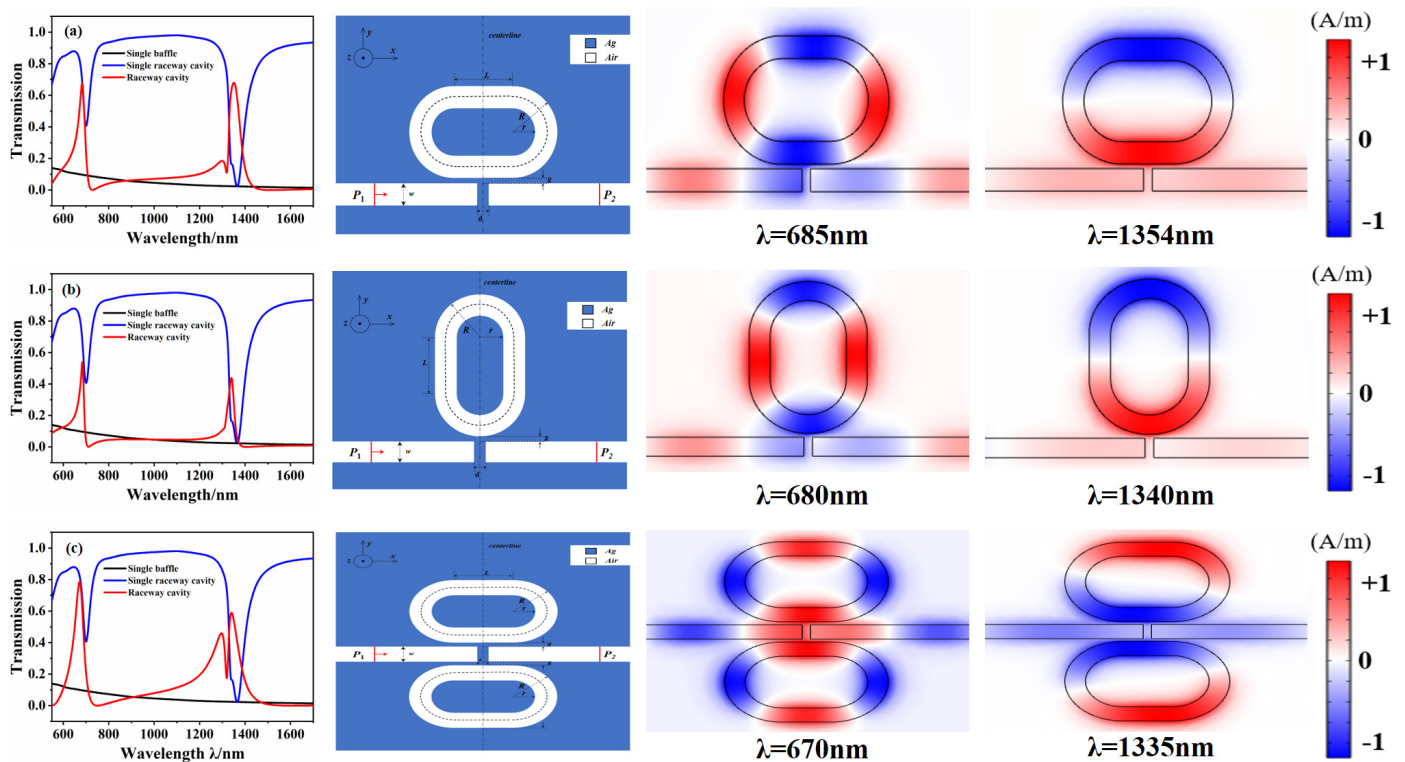


Figure 3. Transmission spectrum, structure diagram, and the Hz field distribution diagram of resonance point of RTRC under different placement methods. (a) Horizontal placement. (b) Vertical placement. (c) Symmetrical placement.

The transmission spectrum of the sensing system when placed horizontally is shown in Figure 3a. When the sensor system (red line) is at $\lambda = 685 \text{ nm}$ and $\lambda = 1354 \text{ nm}$, a sharp asymmetric line is observed, which rapidly drops from the peak to the trough. This is a typical Fano resonance phenomenon. Here, the sensor system is disassembled into two structures, and the formation principle of Fano resonance is analyzed. The transmission spectrum for the structure of the coupled RTRC on the side of the MIM waveguide without baffle is represented by the blue solid line. The analysis showed a narrower transmittance inclination angle, which appeared as a discrete state. Conversely, the transmission spectrum for the baffled MIM waveguide with an RTRC-free structure is represented by the black solid line. A broad and continuous transmission spectrum is shown, with a negative slope and a low transmittance. The Fano phenomenon can therefore be explained by the interaction between a wide, continuous state and a narrow, discrete state. The peaks of Fano resonance are $\lambda = 685 \text{ nm}$ and $\lambda = 1354 \text{ nm}$, and the corresponding magnetic field distribution is also shown in the figure. From the magnetic field distribution, it is concluded that this is a symmetrical mode with $m = 2$ and $m = 1$.

The transmission spectrum of the sensor system when placed vertically is shown in Figure 3b. When the sensor system (red line) is at $\lambda = 680 \text{ nm}$ and $\lambda = 1340 \text{ nm}$, there is also a sharp asymmetrical line that rapidly drops from the peak to the trough. Again, this is typical of the Fano resonance phenomenon, but the resonant peaks have transmittances of 0.54 and 0.42, which are lower than the transmittances of 0.69 and 0.71 in the horizontal placement mode. From the steady-state magnetic field distribution diagram, a symmetrical mode with $m = 2$ and $m = 1$ can be seen. The transmission spectrum of the sensing system when placed symmetrically is shown in Figure 3c. It is clear that the Fano resonance occurs at $\lambda = 670 \text{ nm}$ and $\lambda = 1335 \text{ nm}$. The transmittances of the two resonance peaks are 0.78 and 0.59, which are better than those of the vertical placement method, but the values are generally lower than those of the horizontal placement method. The magnetic field distribution diagram shows that the two resonance peaks, $\lambda = 685 \text{ nm}$ and $\lambda = 1340 \text{ nm}$, correspond to the symmetric mode with $m = 2$ and $m = 1$.

The analysis shows that the introduction of the track structure can achieve a double Fano resonance. Different placement methods can affect the Fano resonant peak, whereas the position of the resonant peak is less affected. Simultaneously, the Fano resonant peak is sharper in the horizontal placement mode. In the subsequent discussion, the processing technology was mainly based on the structure in the horizontal placement mode.

3. Structural Analysis

The different structural parameters of the racetrack resonant cavity affect the position of the resonant peak and its peak value. Therefore, the transmission characteristics of the sensing system are related to the geometric parameters of the structure, meaning the transmission spectra under different structural parameters must be analyzed. The performance of the sensing system generally has two important evaluation indicators, usually expressed by S and FOM [23]:

$$S = \frac{\Delta\lambda}{\Delta n} (nm/RIU) \tag{8}$$

$$FOM = \frac{S}{FWHM} \tag{9}$$

where Δn is the change in refractive index, $\Delta\lambda$ is the change in the resonance wavelength, and FWHM is the full width at half maximum.

The refractive index-sensing performance of the structure was analyzed by calculating the system transmission spectra under different refractive indices n . The structural parameters of the waveguide were the same as those in Figure 1, and the refractive index was increased from 1 to 1.20 in intervals of 0.05. Figure 4a shows the transmission spectra of the waveguide structure under different media refractive indices. As shown in the figure, the Fano resonances in both modes of the transmission spectra show a redshift as the refractive index n increases.

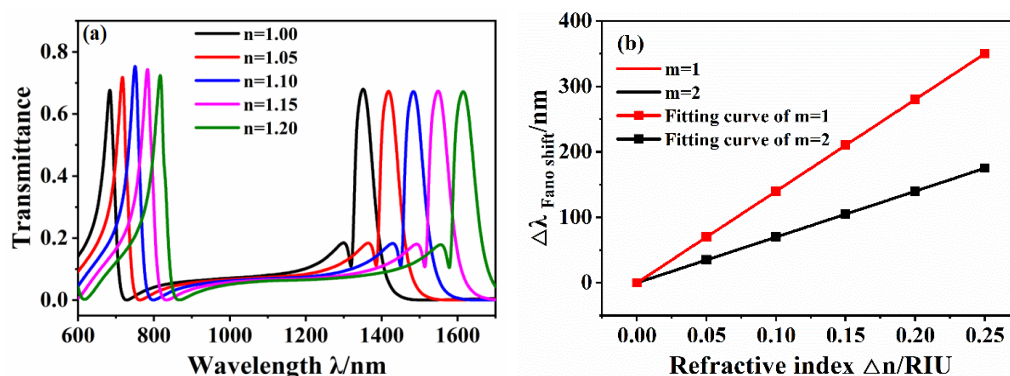


Figure 4. (a) Transmission spectrum of waveguide structure under different refractive index n . (b) Sensitivity fitting curve.

The sensitivity of using the linear fitting of the two symmetrical modes is shown in Figure 4b. The sensitivity of symmetrical mode $m = 1$ is 1401.3 nm/RIU, FWHM = 53.0 nm, with FOM = 26.4, and the sensitivity of symmetrical mode $m = 2$ is 701.2 nm/RIU, FWHM = 15.14 nm, with FOM = 46.31. The analysis results show that the structure has a higher sensitivity as a refractive index sensor and can therefore be used in the field of refractive index sensing. The comparison shows that the sensitivity and FOM in the $m = 1$ mode are higher, and the symmetric mode $m = 1$ is discussed later.

Other structural parameters of the fixed waveguide structure remained unchanged, such that $L = 120$ nm, $g = 10$ nm, and $d = 20$ nm, and the outer diameter R of the RTRC was increased from 120 nm to 160 nm in intervals of 10 nm to investigate the influence of a single variable—the RTRC outer diameter—on the transmission spectrum. The transmission spectra of the structure under different outer diameters were obtained from the simulation,

as shown in Figure 5a. With an increase in R , the Fano resonance exhibits a significant redshift. The $m = 1$ mode corresponds to a weakening Fano resonance peak. This is attributed to the change in R affecting the change in the narrowband mode, where this corresponding change in the narrowband mode leads to changes in the position and transmittance of the Fano resonance [33]. The change in the Fano resonance peak with the refractive index Δn under the symmetry mode $m = 1$ is shown in Figure 5b. When $R = 160$ nm, the maximum sensitivity can reach 1440 nm/RIU, and the FOM is 27.

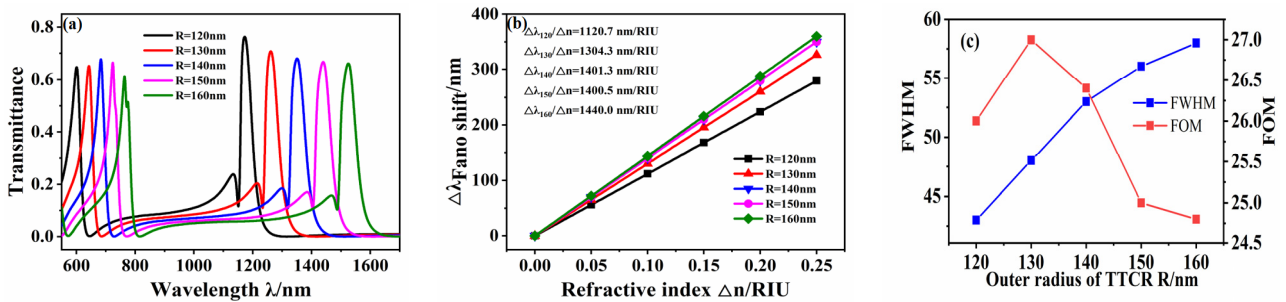


Figure 5. (a) Transmission spectrum of waveguide structure under different R . (b) Sensitivity fitting curve. (c) Fitting curve of FWHM and FOM values.

In addition, the introduced racetrack structure affects the transmission performance of the sensing system, and therefore, its size parameters are analyzed. The length L of the racetrack was increased from 80 nm to 160 nm in intervals of 20 nm, and other parameters were fixed at $R = 140$ nm, $g = 10$ nm, and $d = 20$ nm. The transmission spectra of the sensor system for different racetrack lengths are shown in Figure 6a. With an increase in L , the Fano resonance produces a significant redshift, and the intensity of the Fano resonance peak on the right gradually decreases. This is because the position of the Fano resonance is determined by the narrowband discrete state, and the increase in L triggers a decrease in the resonance wavelength of the narrowband spectrum, so that the Fano resonance produces a redshift. The wavelength drift of the Fano resonance peak with the refractive index Δn under symmetry mode $m = 1$ is shown in Figure 6b. After fitting, the maximum sensitivity of the system reaches 1503.7 nm/RIU when $L = 160$ nm, and the FOM is 26.8.

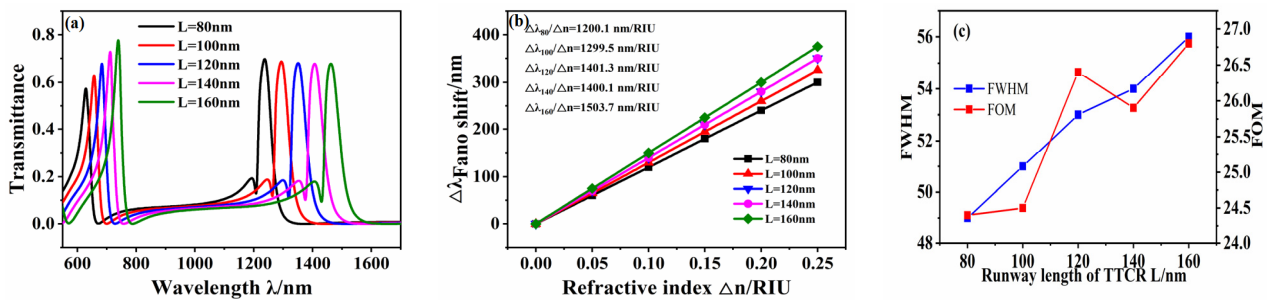


Figure 6. (a) Transmission spectrum of waveguide structure under different L . (b) Sensitivity fitting curve. (c) Fitting curve of FWHM and FOM values.

The width of the introduced baffle also affects the transmission spectrum of the sensor system. The other parameters were fixed at $R = 140$ nm, $r = 90$ nm, $L = 120$ nm, and $g = 10$ nm, and the baffle width d was increased from 10 nm to 30 nm in intervals of 5 nm. The transmission spectra under different baffle widths were simulated, as shown in Figure 7a. As the baffle width d increases, there is no significant change in the position of the Fano resonance peak. The fitting curve of the displacement of the Fano peak with the refractive index Δn under the symmetry mode $m = 1$ is shown in Figure 7b, which illustrates that the sensitivity of the sensor system only slightly changes with the increase in d . The FWHM first increases and then decreases, and the FOM value does not change significantly, indicating that the baffle width has little effect on the sensitivity.

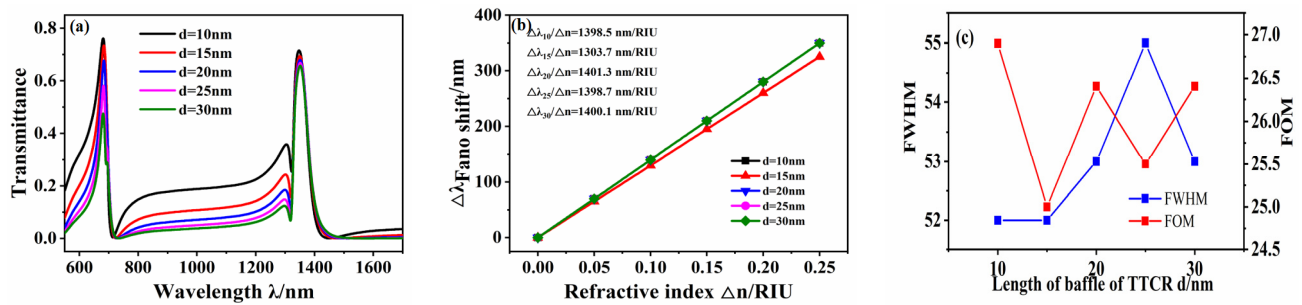


Figure 7. (a) Transmission spectrum of waveguide structure under different d . (b) Sensitivity fitting curve. (c) Fitting curve of FWHM and FOM values.

By analyzing the transmission spectrum lines under different radii R , racetrack lengths L , and baffle widths, the influence of these parameters on the sensing system could be investigated. The results show that the transmission spectrum line is most significantly influenced by the radius R and the racetrack length L . The width did not affect the transmission spectra. When $R = 160$ nm, the sensitivity of the sensing system reaches a maximum of 1503.7 nm/RIU. Compared with previous studies, as shown in Table 1, the designed sensor has the advantage of high sensitivity when applied to refractive index sensing.

Table 1. The RI sensitivity reported in references.

References	Structure	Sensitivity (nm/RIU)	FOM (RIU ⁻¹)	Resonant Wave Length (nm)
[21]	Cup cavity	600	120	600–1200
[23]	Notched cavity	1071	12.5	500–1700
[22]	Splitting ring cavity	1200	12.2	800–1450
[24]	Multiple ring cavity	1217	24.34	500–1200
[34]	Rectangular cavity	985	25	600–1000
[35]	Multi-sided ring cavity	1949	29.52	100–1600
[36]	Nano ring cavity	2080	29.92	1800–2600
This study	TTCRC	1503.7	26.8	600–1500

4. Sensing Application

The waveguide and the RTRC structure are filled with high-refractive-index temperature coefficient materials, and the application of the proposed structure in the field of temperature sensing is explored. Ethanol is the selected filling material owing to its high-refractive-index temperature coefficient (3.94×10^{-4}), which far exceeds that of Ag (9.30×10^{-6}) and the substrate material SiO₂ (8.60×10^{-6}), and there is an unambiguous linear relationship between the refractive index of ethanol and the temperature:

$$n = 1.36048 - 3.94 \times 10^{-4}(T - T_0) \tag{10}$$

where T_0 is the room temperature taken to be 20 °C, and T is the surrounding temperature to be measured [37]. The variation in the outside temperature mainly affects ethanol, hence the waveguide and RTRC are filled with ethanol. The sensitivity of temperature sensing can be defined as $S_T = \Delta\lambda/\Delta T$, where $\Delta\lambda$ is the shift in wavelength and ΔT is the variation in temperature. The geometrical parameters of the structure are consistent with those shown in Figure 1.

The transmission spectra of the structures at different temperatures are shown in Figure 8a. As the temperature increases, the Fano resonance produces a blueshift with an increase in the refractive index. The line type of the Fano resonance remains unchanged, and the height of the resonance peak does not change significantly. According to Equation (9), the temperature is inversely proportional to the refractive index. The Fano resonance is redshifted as the refractive index increases, meaning the Fano resonance is blueshifted as the temperature increases. In addition, the sensitivity fitting curve of the temperature

sensor is shown in Figure 8b, and the temperature sensitivity is 0.75 nm/°C. Comparisons with previous studies, as shown in Table 2, show that the designed structure has the advantage of high sensitivity when applied to temperature sensing.

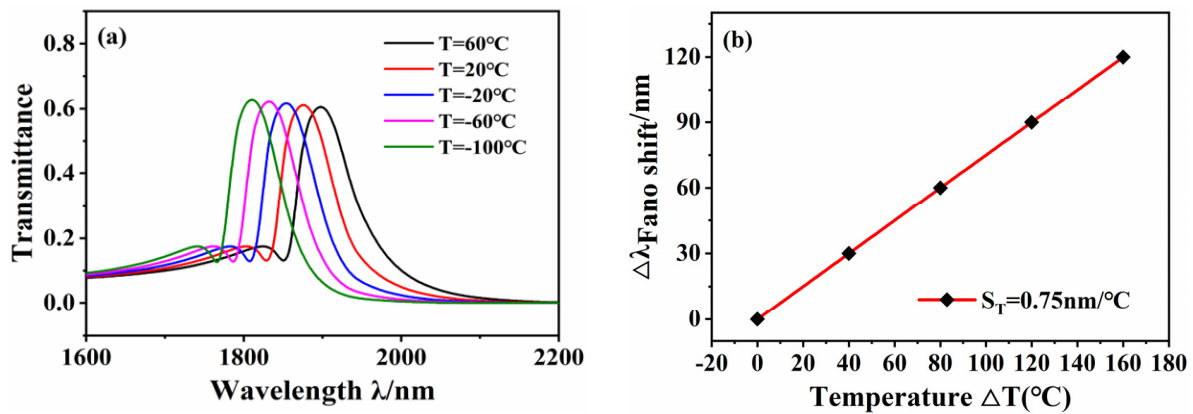


Figure 8. (a) Transmission spectrum at different temperatures. (b) Temperature sensitivity fitting curve.

Table 2. The temperature sensitivity reported in references.

References	Structure	Temperature Sensitivity (nm/°C)	Resonant Wavelength (nm)	Sensitive Material
[38]	Fiber-optical sensor	0.073	1500–1600	Water
[39]	Fiber-optical sensor	0.059	1500–1600	Sodium chloride
[40]	Ring cavity	0.62	2600–4400	Ethanol
[41]	Circular cavity	0.664	800–2000	Ethanol
[42]	Array cavity	0.84	800–4000	Ethanol
This study	TCRC	0.75	1600–2200	Ethanol

5. Conclusions

In summary, this study proposed a sensing system coupled with a baffled MIM waveguide and a racetrack resonant cavity, which was analyzed using the finite element method. The results show that the waveguide structure can achieve double Fano resonance, and different placement methods affect the resonant peak of the sensing system. The design structural parameters, such as radius and racetrack length, simultaneously affect the position and peak values of the Fano resonance peak. In addition, the performance of the sensor is optimized by controlling the geometric parameters. The results show that when the sensing system is used in the field of refractive index sensing, the sensitivity can reach 1503.7 nm/RIU, and the FOM is 26.8; when applied to temperature sensing, the sensitivity can reach 0.75 nm/°C, which is 10 times higher than that of the same type of fibre-optic sensor. It is 10 times more sensitive than the same type of fibre optic sensor. This study introduces a runway structure and a stub structure, which, compared to the regular ring structure, does not require any change in the radius of the resonant cavity, and only requires a dimensional adjustment of the introduced runway to meet the requirements of some special size devices, compared to other ring structures, such as the introduction of defects, stubs, etc. The proposed structure is more compact to prepare and the preparation process is less difficult, thus offering potential for application in the field of optical integration.

Author Contributions: Conceptualization, Y.Y.; methodology, Y.Y.; software, J.C.; formal analysis, G.Z.; investigation, G.L.; resources, R.Z.; data curation, M.Z.; writing—original draft preparation, Y.Y.; writing—review and editing, Y.Y. Additionally, supervision, Y.Y.; project administration, G.Z.; funding acquisition, W.Z. All authors have read and agreed to the published version of the manuscript.

Funding: This work was supported by National Key Research and Development Project (Grant No.2019YFC0119800), National Natural Science Foundation of China (Grant No.51875535), National Natural Science Foundation of China as National Major Scientific Instruments Development Project (Grant No. 61927807), and the Fund for Shanxi 1331 Project Key Subject Construction and Innovation Special Zone Project.

Data Availability Statement: The available data has been stated in the article.

Acknowledgments: The system numerical simulation was provided by COMSOL, Multiphysics.

Conflicts of Interest: The authors declare no conflict of interest.

References

1. Barnes, W.L.; Dereux, A.; Ebbesen, T.W. Surface Plasmon Subwavelength Optics. *Nature* **2003**, *424*, 824–830. [[CrossRef](#)] [[PubMed](#)]
2. Yue, T.; Zhang, Z.; Wang, R. Refractive Index Sensor Based on Fano Resonances in Metal-Insulator-Metal Waveguides Coupled with Resonators. *Sensors* **2017**, *17*, 784.
3. Hsieh, L.Z.; Chau, Y.; Lim, C.M. Metal nano-particles sizing by thermal annealing for the enhancement of surface plasmon effects in thin-film solar cells application. *Opt. Commun.* **2016**, *370*, 85–90. [[CrossRef](#)]
4. Sung, M.J.; Ma, Y.F.; Chau, Y.F. Surface plasmon resonance in a hexagonal nanostructure formed by seven core shell nanocylinders. *Appl. Opt.* **2010**, *49*, 920–926. [[CrossRef](#)]
5. Chau, Y.F.; Jiang, Z.H. Plasmonics Effects of Nanometal Embedded in a Dielectric Substrate. *Plasmonics* **2011**, *6*, 581–589. [[CrossRef](#)]
6. Sarkaleh, A.K.; Lahijani, B.V.; Saberkari, H. Optical Ring Resonators: A Platform for Biological Sensing Applications. *J. Med. Signals Sens.* **2017**, *7*, 185–191. [[CrossRef](#)] [[PubMed](#)]
7. Tsigaridas, G.N. A study on refractive index sensors based on optical micro-ring resonators. *Photonic Sens.* **2017**, *3*, 217–225. [[CrossRef](#)]
8. Zhang, Z.; Shi, F.; Chen, Y. Tunable Multichannel Plasmonic Filter Based on Coupling-Induced Mode Splitting. *Plasmonics* **2015**, *10*, 139–144. [[CrossRef](#)]
9. Wang, S.; Li, Y.; Xu, Q. A MIM Filter Based on a Side-Coupled Crossbeam Square-Ring Resonator. *Plasmonics* **2016**, *11*, 1291–1296. [[CrossRef](#)]
10. Ma, F.S.; Lee, C. Optical Nanofilters Based on Meta-Atom Side-Coupled Plasmonics Metal-Insulator-Metal Waveguides. *J. Lightwave Technol.* **2013**, *31*, 2876–2880. [[CrossRef](#)]
11. Veronis, G.; Fan, S. Bends and splitters in metal-dielectric-metal subwavelength plasmonic waveguides. *Appl. Phys. Lett.* **2005**, *87*, 131101–131103. [[CrossRef](#)]
12. Lin, W.; Wei, L. Tunable control of electromagnetically induced transparency analogue in a compact graphene-based waveguide. *Opt. Lett.* **2015**, *40*, 2325–2328.
13. Li, H.J.; Wang, L.L.; Xiang, Z. Plasmonically Induced Absorption and Transparency Based on MIM Waveguides with Concentric Nanorings. *IEEE Photonic Technol. Lett.* **2016**, *28*, 1454–1457. [[CrossRef](#)]
14. Gao, Y.; Zhan, S.; Liu, Q.; Liu, Y. Controllable plasmonic sensing based on Fano resonance in a cavity coupled defective MDM waveguide. *J. Phys. D Appl. Phys.* **2016**, *49*, 265109. [[CrossRef](#)]
15. Miroshnichenko, A.E.; Flach, S.; Kivshar, Y.S. Fano resonances in nanoscale structures. *Rev. Mod. Phys.* **2009**, *82*, 2257–2298. [[CrossRef](#)]
16. Qi, J.; Chen, Z.; Chen, J. Independently tunable double Fano resonances in asymmetric MIM waveguide structure. *Opt. Express* **2014**, *22*, 14688–14695. [[CrossRef](#)]
17. Pang, S.; Huo, Y.; Xie, Y.; Hao, L. Tunable Electromagnetically Induced Transparency-Like in Plasmonic Stub Waveguide with Cross Resonator. *Plasmonics* **2017**, *12*, 1161–1168. [[CrossRef](#)]
18. Mirin, N.A.; Bao, K.; Nordlander, P. Fano Resonances in Plasmonic Nanoparticle Aggregates. *J. Phys. Chem. A* **2009**, *113*, 4028–4034. [[CrossRef](#)] [[PubMed](#)]
19. Chang, W.S.; Lassiter, J.B.; Swanglap, P. A Plasmonic Fano Switch. *Nano Lett.* **2012**, *12*, 4977–4982. [[CrossRef](#)]
20. Li, Z.; Cakmakyapan, S.; Butun, B. Fano resonances in THz metamaterials composed of continuous metallic wires and split ring resonators. *Opt. Express* **2014**, *22*, 26572–26584. [[CrossRef](#)]
21. Zi-Hua, L.; Zheng, L. Plasmonics refractive index sensor based on tunable ultra-sharp Fano resonance. *Optoelectron. Lett.* **2018**, *14*, 421–424.
22. Zhang, Y.; Kuang, Y.; Zhang, Z. High-sensitivity refractive index sensors based on Fano resonance in the plasmonic system of splitting ring cavity-coupled MIM waveguide with tooth cavity. *Appl. Phys.* **2019**, *125*, 13. [[CrossRef](#)]
23. Yang, J.; Song, X.; Chen, Z. Tunable Multi-Fano Resonances in MDM-Based Side-Coupled Resonator System and its Application in Nanosensor. *Plasmonics* **2017**, *12*, 1665–1672. [[CrossRef](#)]
24. Manolatu, C.; Khan, M.J.; Fan, S. Coupling of modes analysis of resonant channel add-drop filters. *IEEE J. Quantum Electron.* **1999**, *35*, 1322–1331. [[CrossRef](#)]

25. Liu, D.; Fu, W. Plasmon-Induced Transparency and Refractive Index Sensing Based on a Trapezoid Cavity Coupled with a Hexagonal Resonator. *Plasmonics* **2019**, *14*, 663–671. [[CrossRef](#)]
26. Zhao, C.; Song, X.; Duan, G. Multiple Fano Resonances Control in MIM Side-Coupled Cavities Systems. *IEEE Photonics J.* **2015**, *7*, 1–10.
27. Chen, F.; Zhang, H.; Sun, L. Temperature tunable Fano resonance based on ring resonator side coupled with a MIM waveguide. *Opt. Laser Technol.* **2019**, *116*, 293–299. [[CrossRef](#)]
28. Chou, Y.F.; Chao, C.; Huang, H.J. Ultrawide Bandgap and High Sensitivity of a Plasmonic Metal-Insulator-Metal Waveguide Filter with Cavity and Baffles. *Nanomaterials* **2020**, *10*, 2030. [[CrossRef](#)]
29. Zhu, J.; Lou, J. High-sensitivity Fano resonance temperature sensor in MIM waveguides coupled with a polydimethylsiloxane-sealed semi-square ring resonator. *Results Phys.* **2020**, *18*, 103183. [[CrossRef](#)]
30. Wu, T.; Liu, T. A nanometric temperature sensor based on plasmonic waveguide with an ethanol-sealed rectangular cavity. *Opt. Commun.* **2015**, *339*, 1–6. [[CrossRef](#)]
31. Kekatpure, R.D.; Hryciw, A.C.; Barnard, E.S. Solving dielectric and plasmonic waveguide dispersion relations on a pocket calculator. *Opt. Express* **2009**, *17*, 24112–24129. [[CrossRef](#)] [[PubMed](#)]
32. Gai, H.; Wang, J.; Qian, T. Modified Debye model parameters of metals applicable for broadband calculations. *Appl. Opt.* **2007**, *46*, 2229–2233. [[CrossRef](#)] [[PubMed](#)]
33. Chau, Y.F.C.; Chou, C.C.T. Improved Refractive Index-Sensing Performance of Multimode Fano-Resonance-Based Metal-Insulator-Metal Nanostructures. *Nanomaterials* **2021**, *11*, 2097. [[CrossRef](#)]
34. Chen, Y.; Chen, L.; Wen, K. Multiple fano resonances in a coupled plasmonic resonator system. *J. Appl. Phys.* **2019**, *126*, 083102. [[CrossRef](#)]
35. Butt, M.A.; Kazanskiy, N.L.; Khonina, S.N. Highly integrated plasmonic sensor design for the simultaneous detection of multiple analytes. *Curr. Appl. Phys.* **2020**, *20*, 1274–1280. [[CrossRef](#)]
36. Chao, C. Highly Sensitive and Tunable Plasmonic Sensor Based on a Nanoring Resonator with Silver Nanorods. *Nanomaterials* **2020**, *10*, 1399. [[CrossRef](#)]
37. Yan, S.; Zhang, M. Refractive Index Sensor Based on a Metal-Insulator-Metal Waveguide Coupled with a Symmetric Structure. *Sensors* **2017**, *17*, 2879. [[CrossRef](#)]
38. Fan, J.; Zhang, J.; Ping, L. A single-mode fiber sensor based on core-offset inter-modal interferometer. *Opt. Commun.* **2014**, *320*, 33–37. [[CrossRef](#)]
39. Xuguang, H. Simultaneous measurement of refractive index and temperature based on asymmetric structures modal interference. *Opt. Commun.* **2016**, *364*, 191–194.
40. Al-Mahmod, M.J.; Hyder, R.; Islam, M.Z. Numerical studies on a plasmonic temperature nanosensor based on a metal-insulator-metal ring resonator structure for optical integrated circuit applications. *Photonic Nanostruct.* **2017**, *25*, 52–57. [[CrossRef](#)]
41. Xie, Y.; Huang, Y.; Xu, W. A Plasmonic Temperature-Sensing Structure Based on Dual Laterally Side-Coupled Hexagonal Cavities. *Sensors* **2016**, *16*, 706. [[CrossRef](#)] [[PubMed](#)]
42. Rakhshani, M.R. High sensitivity plasmonic refractive index sensing and its application for human blood group identification. *Sens. Actuators B-Chem.* **2017**, *249*, 168–176. [[CrossRef](#)]